Taylor & Francis
Taylor & Francis Group

OPEN ACCESS

Electrostatic field analysis of anisotropic conductive media using voxel-based static method of moments with fast multipole method

S. Hamada

Department of Electrical Engineering, Kyoto University, Kyoto, Japan

ABSTRACT

A voxel-based static method of moments (MoM) is proposed to analyse electrostatic fields in biological tissues with anisotropic conductivities, such as nerve fibre. This MoM emulates a volume element by using surface elements and boundary equations; thus, it is regarded as a type of indirect boundary element method (IBEM). Therefore, the MoM can be concurrently applied with the voxel-based IBEM, and both methods can be accelerated by the fast multipole method and fast Fourier transform in the same manner. After validating the MoM, we calculate the magnetically induced electric field in a simplified human head model constructed using diffusion tensor imaging data. It is confirmed that the proposed voxel-based MoM is applicable to field analyses of voxel models composed of isotropic and anisotropic tissues. In addition, by analysing variants of the original inhomogeneous anisotropic model, we observe the variation in the electric current distributions in (i) an inhomogeneous isotropic model, (ii) a homogeneous isotropic model and (iii) an inhomogeneous anisotropic model with finer voxel size. The calculated electric currents in these models exhibit qualitatively reasonable distributions. The proposed method is applied to models with up to 188,296,465 unknowns using a personal computer.

1. Introduction

Numerical electromagnetic field analyses based on voxel models are widely conducted using various methods such as the finite difference method and the finite element method (FEM; Dawson, Caputa, & Stuchly, 1997; Hirata et al., 2010; Rullmann et al., 2009). The advantages of voxel-based analysis include facile production of realistic models from three-dimensional image data and a simple data structure that is suitable for storage, handling and visualisation. A typical application is field analysis of an anatomical human model constructed using magnetic resonance imaging (MRI) data (Nagaoka et al., 2004).

Some biological tissues, such as nerve fibre, muscle and bone, have anisotropic conductivities. For example, high and low conductivities are observed along and across nerve fibre bundles, respectively. Their isotropic approximations can produce field inaccuracies. By considering anisotropy, for example, FEM analyses were conducted using head models based on diffusion tensor imaging (DTI) data (Rullmann et al., 2009; Wolters et al., 2006). DTI is a type of MRI that visualises the apparent diffusion tensor $\mathbf{D}_a$ of water molecules inside the tissues. Conductivity tensors are then approximately estimated using $\mathbf{D}_a$.

On the other hand, a voxel-based indirect boundary element method (IBEM), which uses the Laplace kernel fast multipole method (FMM) (Greengard & Rokhlin, 1997) to handle large-scale problems, was developed by Hamada and Kobayashi (2006). This method analyses the electrostatic fields in cubic voxel models that describe the conductivities of biological tissues. The quality of the calculated field is comparable to that obtained using the scalar-potential finite-difference method, impedance method and quasi-static finite-difference time-domain method (Hirata et al., 2010). Moreover, this method can effectively manage a voxel model composed of 547 million tissue voxels and 61 million boundary elements using a personal computer (Hamada, 2014a, 2014b). However, it cannot address anisotropic conductivities.

In this study, in order to enhance the versatility of the voxel-based IBEM, the static method of moments (MoM; Cadebec, Coulomb, & Janet, 2006; Newman, Trowbridge, & Turner, 1972; Takahashi, Wakao, & Kameari, 2006) is remodelled into a voxel-based static MoM, which is designed to address anisotropic conductivities. This MoM emulates a volume element by using surface elements and boundary equations. It does not execute volume integrals; thus, it is regarded as a type of IBEM. Therefore, the MoM can be concurrently applied with the voxel-based IBEM, and both methods can be accelerated by the FMM and the fast Fourier transform (FFT) in the same manner. After validating this MoM, we calculate the electrostatic field in a simplified human head model including inhomogeneous anisotropic conductive tissues, which is developed using DTI data. In addition, we observe the variation in the calculated field distributions in three variants of the original model. It is shown that the proposed MoM and the IBEM are concurrently applicable to field analyses of voxel models composed of isotropic and anisotropic tissues.

2. Voxel-based indirect BEM and voxel-based static MoM

2.1. Magnetically induced electrostatic field in biological samples

The basic equations of magnetically induced low-frequency faint currents in a biological sample have been provided by, for example, Dawson et al. (1997). Here, both the displacement current and the secondary magnetic field are assumed to be negligible. When an external vector potential $\boldsymbol{A}_0$ and a magnetic flux density

B_0, which satisfy $B_0 = \nabla \times A_0$, are applied, the magnetically induced electric field E and the electric current density J satisfy the following equations:

$$E = -\mathrm{j}\omega A_0 - \nabla\varphi, \ J = \sigma E, \ \nabla^2\varphi = 0, \tag{1}$$

where j, ω, σ and φ are the imaginary unit, angular frequency, conductivity and electric scalar potential, respectively. The following boundary equation (BEQ) holds for a boundary with a unit normal vector n:

$$\sigma_+ E_+ \cdot n = \sigma_- E_- \cdot n. \tag{2}$$

The subscripts $+$ and $-$ indicate the positive and negative sides with respect to n, respectively. This BEQ is equivalent to the following pair of BEQs, each of which is described using quantities defined on one side of the boundary:

$$s_+ = -\sigma_0\left(\sigma_{r+} - 1\right)E_+ \cdot n, \ s_- = +\sigma_0\left(\sigma_{r-} - 1\right)E_- \cdot n, \ \sigma_\pm = \sigma_0\sigma_{r\pm}, \tag{3}$$

where s, σ_r and σ_0 are the surface charge density, relative conductivity and an arbitrary scalar reference value of conductivity, respectively. These quantities are analogous to those describing magnetisation or dielectric polarisation. Note that Equation (3) dissolves the direct relationship between quantities defined on the plus and minus sides of the boundary.

Anisotropic conductivity is represented by regarding σ and σ_r as second-order tensors $\boldsymbol{\sigma}$ and $\boldsymbol{\sigma}_r$, respectively.

$$\boldsymbol{\sigma}_r = \begin{pmatrix} \sigma_{rxx} & \sigma_{rxy} & \sigma_{rxz} \\ \sigma_{rxy} & \sigma_{ryy} & \sigma_{ryz} \\ \sigma_{rxz} & \sigma_{ryz} & \sigma_{rzz} \end{pmatrix} = \mathbf{ACA}^{\mathrm{T}} + \mathbf{I}, \ \mathbf{A} = \begin{pmatrix} u_x & v_x & w_x \\ u_y & v_y & w_y \\ u_z & v_z & w_z \end{pmatrix},$$

$$\mathbf{C} = \begin{pmatrix} \sigma_{ru} - 1 & 0 & 0 \\ 0 & \sigma_{rv} - 1 & 0 \\ 0 & 0 & \sigma_{rw} - 1 \end{pmatrix}, \tag{4}$$

where the superscript T denotes the transpose, and σ_{rxx}, σ_{rxy}, σ_{rxz}, σ_{ryy}, σ_{ryz} and σ_{rzz} are the components of tensor $\boldsymbol{\sigma}_r$ in the xyz coordinate system. The vectors $u = (u_x, u_y, u_z)^{\mathrm{T}}$, $v = (v_x, v_y, v_z)^{\mathrm{T}}$ and $w = (w_x, w_y, w_z)^{\mathrm{T}}$ are the unit eigenvectors of $\boldsymbol{\sigma}_r$, and σ_{ru}, σ_{rv}, and σ_{rw} are the eigenvalues in the corresponding directions.

2.2. Voxel-based indirect boundary element method

The voxel-based IBEM regards a square boundary sandwiched by two voxels having different conductivities as a square boundary element (Hamada & Kobayashi, 2006). The element has uniform surface charge density and numerically simulates

φ in Equation (1). Here, $\boldsymbol{n}$ is restricted to $\boldsymbol{i}, \boldsymbol{j}$ or $\boldsymbol{k}$, which are parallel to the x, y and z axes, respectively. Equation (2) produces the following BEQ for the IBEM:

$$\sigma_0 \sigma_{r+} \overline{E_{n+}} = \sigma_0 \sigma_{r-} \overline{E_{n-}}, \quad \overline{E_{n\pm}} = \int_S \boldsymbol{E}_\pm \cdot \boldsymbol{n} dS / \ell^2, \tag{5}$$
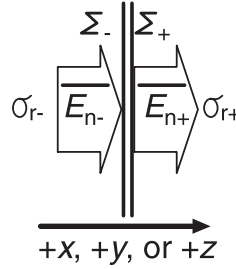
where ℓ is the voxel side length and S denotes the area of a surface element. Similarly, Equation (3) provides the following BEQs, which are equivalent to Equation (5):

$$\overline{s_+} = -\sigma_0 (\sigma_{r+} - 1) \overline{E_{n+}}, \quad \overline{s_-} = +\sigma_0 (\sigma_{r-} - 1) \overline{E_{n-}}, \quad \overline{s_\pm} = \int_S s_\pm dS / \ell^2. \tag{6}$$
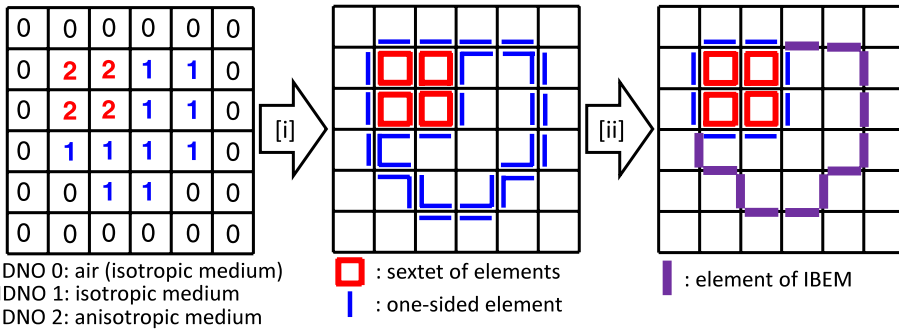
Let us approximate $\overline{s_\pm}$ by the uniform charge densities $\Sigma_\pm$ of the surface charge elements as follows:

$$\Sigma_+ = -\sigma_0 (\sigma_{r+} - 1) \overline{E_{n+}}, \quad \Sigma_- = +\sigma_0 (\sigma_{r-} - 1) \overline{E_{n-}}. \tag{7}$$

Note that Σ_+ and Σ_- are governed by these BEQs, each of which is described using quantities defined on only one side of the elements, and we refer to these

Figure 1. Pair of one-sided elements.

IDNO 0: air (isotropic medium)
IDNO 1: isotropic medium
IDNO 2: anisotropic medium

□ : sextet of elements
❙ : one-sided element

❚ : element of IBEM

Figure 2. Two-dimensional schematic arrangement of elements for voxel model involving isotropic and anisotropic media.

elements as one-sided elements (see Figure 1). The surface charge density of the IBEM element equals the sum of Σ_+ and Σ_- when they are in the same position.

Now, the IBEM elements can also be allocated using the following procedures (see Figure 2):

[i] The one-sided elements are allocated to cover each isotropic medium that is represented as a voxel cluster. The non-conductive open region outside the tissues is also classified as an isotropic voxel cluster.

[ii] A pair of one-sided elements that are in the same position is replaced with an IBEM element.

2.3. Voxel-based static method of moments

We propose a voxel-based static MoM, which represents a cubic voxel of an anisotropic medium using a sextet of one-sided elements defined on the inner surfaces of the voxel (see Figures 2 and 3). It is assumed that the surface charge densities, Σ_1 through Σ_6, in Figure 3 are approximately evaluated by the following equations using $\overline{E}_{n1}$ through $\overline{E}_{n6}$, similarly to the way $\Sigma_\pm$ are evaluated by $\overline{E}_{n\pm}$ in Equation (7):

$$
\begin{pmatrix} \Sigma_1 \\ \Sigma_2 \\ \Sigma_3 \\ \Sigma_4 \\ \Sigma_5 \\ \Sigma_6 \end{pmatrix} = \sigma_0 \begin{pmatrix} \dfrac{\mathbf{ACA}^{\mathrm{T}}+\mathbf{Y}}{2} - \dfrac{\mathbf{Z}}{6} & \dfrac{\mathbf{ACA}^{\mathrm{T}}-\mathbf{Y}}{2} + \dfrac{\mathbf{Z}}{6} \\ \dfrac{-\mathbf{ACA}^{\mathrm{T}}+\mathbf{Y}}{2} - \dfrac{\mathbf{Z}}{6} & \dfrac{-\mathbf{ACA}^{\mathrm{T}}-\mathbf{Y}}{2} + \dfrac{\mathbf{Z}}{6} \end{pmatrix} \begin{pmatrix} \overline{E}_{n1} \\ \overline{E}_{n2} \\ \overline{E}_{n3} \\ \overline{E}_{n4} \\ \overline{E}_{n5} \\ \overline{E}_{n6} \end{pmatrix}
$$

$$
\mathbf{Y} = \begin{pmatrix} \sigma_{\mathrm{r}xx} - 1 & 0 & 0 \\ 0 & \sigma_{\mathrm{r}yy} - 1 & 0 \\ 0 & 0 & \sigma_{\mathrm{r}zz} - 1 \end{pmatrix}, \ \mathbf{Z} = \begin{pmatrix} \sigma_{\mathrm{r}xx} - 1 & \sigma_{\mathrm{r}yy} - 1 & \sigma_{\mathrm{r}zz} - 1 \\ \sigma_{\mathrm{r}xx} - 1 & \sigma_{\mathrm{r}yy} - 1 & \sigma_{\mathrm{r}zz} - 1 \\ \sigma_{\mathrm{r}xx} - 1 & \sigma_{\mathrm{r}yy} - 1 & \sigma_{\mathrm{r}zz} - 1 \end{pmatrix}, \ (8)
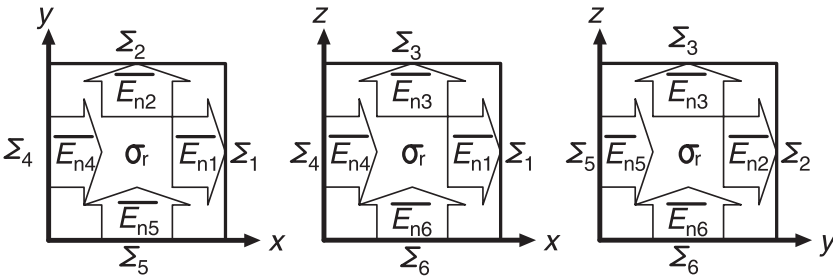$$

Figure 3. Sextet of one-sided elements for anisotropic voxel.

where the $\mathbf{ACA}^{\mathrm{T}}$ and $\mathbf{Y}$ terms describe, for example, the following relationship:

$$\Sigma_1 = \sigma_0(\sigma_{rxx} - 1)\overline{E_{n1}} + \sigma_0\sigma_{rxy}\left(\overline{E_{n2}} + \overline{E_{n5}}\right)/2 + \sigma_0\sigma_{rxz}\left(\overline{E_{n3}} + \overline{E_{n6}}\right)/2. \quad (9)$$

Equation (9) suggests that the average field on the surface assigned Σ_1 is approximated by $\left(\overline{E_{n1}}, \quad \left(\overline{E_{n2}} + \overline{E_{n5}}\right)/2, \quad \left(\overline{E_{n3}} + \overline{E_{n6}}\right)/2\right)^{\mathrm{T}}$, which is the exact field when ℓ tends to zero. The $\mathbf{Z}$ terms constrain $\sum_{i=1}^{6} \Sigma_i$ to zero, and they vanish when ℓ tends to zero. Although the sum of the polarisation charges is theoretically zero in an arbitrary closed surface, the $\mathbf{Z}$ terms approximately emulate this relationship in the closed surface just covering each voxel. These properties allow Equation (8) to address anisotropy. When the following procedures are added to those listed in the previous section, concurrent use of the voxel-based MoM and IBEM is possible. This is illustrated in Figure 2.

    [i] The sextet of elements is allocated to every anisotropic voxel.

    [ii] The sextet charges cannot be replaced with IBEM elements.

    Supplemental comments are provided in the Appendix.

2.4. Governing simultaneous linear equations

The IBEM elements, one-sided elements and sextet charge elements are collectively rearranged in a new order and assigned a serial number between 1 and N. The charge density of the ith element is denoted by x_i. Considering Coulomb's law and the externally applied field, the $\overline{E_{n\pm}}$ on the ith element, $\overline{E_{n\pm[i]}}$, is represented by the following integral equation:

$$\overline{E_{n\pm[i]}} = -\int_{S_i} j\omega A_0 \cdot n\,dS/\ell^2 + \sum_{j=1, j\neq\{i\}}^{N} \int_{S_i}\left\{\int_{S_j} \frac{x_j\left(r_i - r_j\right)}{4\pi\sigma_0\left|r_i - r_j\right|^3}dS\right\} \cdot n\,dS/\ell^2$$
$$\pm \frac{1}{2\sigma_0}\sum_{k=\{i\}} x_k, \quad\quad\quad\quad\quad\quad\quad\quad\quad\quad (10)$$

where r_i is the position vector on the ith element. If no other element is in the location of the ith element, $\{i\}$ denotes i; otherwise, $\{i\}$ denotes the set containing i and the other element's number if they are in the same position. The governing linear equations, $\mathbf{Cx} = \mathbf{b}$, are derived using Equations (5), (7), (8), and (10), where $\mathbf{C}$, x and b are an $N \times N$ coefficient matrix, $N \times 1$ unknown vector and $N \times 1$ constant vector, respectively. Because this formulation does not involve volume integrals, this MoM is considered to be a type of IBEM. After solving for x, fields E and J are calculated for all the voxel centres. For example, E at the gravity centre of the voxel illustrated in Figure 3 is approximated by $\left(\left(\overline{E_{n1}} + \overline{E_{n4}}\right)/2, \quad \left(\overline{E_{n2}} + \overline{E_{n5}}\right)/2, \quad \left(\overline{E_{n3}} + \overline{E_{n6}}\right)/2\right)^{\mathrm{T}}$, where $E_{n1} - E_{n6}$ are

calculated using Equation (10). The value of *J* at the voxel centre is evaluated by using $J = \sigma E$ or $J = \boldsymbol{\sigma} E$.

2.5. Voxel-based fast multipole method

When we solve the equation $\mathbf{C}x = b$ with an iterative solver, we accelerate the matrix-vector multiplication operation by using the FMM. Because the voxel-based MoM and IBEM use a common set of surface elements defined on the voxel walls, the voxel-based MoM is also accelerated by the voxel-based FMM developed for the voxel-based IBEM. However, the surface elements for this MoM are densely allocated in anisotropic media; thus, the calculation cost of near-field components in the FMM algorithm (Hamada, 2011) tends to be high.

On the other hand, we can adopt the FFT as an alternative to the voxel-based FMM for the multiplication operation. Because the FFT algorithm is efficient when the surface elements are densely allocated, we adopt it to calculate only the near-field components of the voxel-based FMM. This hybrid technique that is applied to the surface elements is similar to that developed by De Zaeytijd, Bogaert, and Franchois (2008) for volume elements using a uniform cubic grid.

3. Simplified human head model constructed using DTI data

In order to analyse electrostatic fields in an anisotropic biological sample, a simplified model of a human head was generated using DTI data (Rullmann et al., 2009; Wolters et al., 2006). DTI is a type of MRI that produces a set of MR images of *in vivo* biological tissues, from which the apparent diffusion tensor $\mathbf{D}_a$ of water molecules inside the tissues can be evaluated for every voxel location. Rullmann presented one of the simplest methods for evaluating the conductivity tensor $\boldsymbol{\sigma}$ from $\mathbf{D}_a$ (Rullmann et al., 2009). This method assumes that $\boldsymbol{\sigma}$ is proportional to $\mathbf{D}_a$ and that the magnitude ratio of $\boldsymbol{\sigma}$ to $\mathbf{D}_a$ equals the ratio of the isotropic conductivity value found in literature to the geometric mean of the three eigenvalues of $\mathbf{D}_a$.

We obtained $\mathbf{D}_a$ data using DTI Studio and DTI sample data of a human head (https://www.mristudio.org). The dimensions of the original $\mathbf{D}_a$ data were $256 \times 256 \times 58$, and they were resized to $88 \times 88 \times 60$. The top and bottom slices were considered to be 'air' slices. The voxel size was set to $2.5 \times 2.5 \times 2.5$ mm^3. Based on T2-weighted MR images, the volume was classified into five regions (see Figure 4): air, outside the skull, skull, inside the skull and eyeballs.

The number of voxels and the average value of the isotropic conductivities found in literature are summarised in Table 1. The average was calculated using the anatomical human voxel model developed by Nagaoka et al. (2004) with the conductivities compiled by Hirata et al. (2010), in which the tissue conductivities range from $V_L = 0.02$ to $V_U = 2.0$ Sm^{-1} (both inclusive), where V_L and V_U are the respective values of the cortical bone and cerebrospinal fluid (CSF).
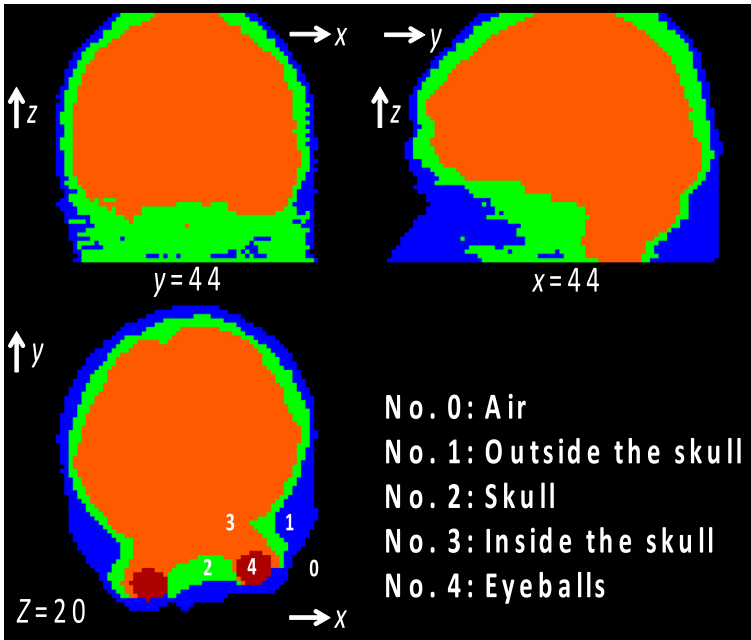
Figure 4. Simplified head model.

Table 1. Number of voxels and average conductivities in developed head model.

ID no.	Region	No. of voxels	Average conductivity/Sm^{-1}
0	Air	287,976	0.00
1	Outside the skull	33,123	0.21
2	Skull	52,881	0.02
3	Inside the skull	89,903	0.47
4	Eyeballs	766	1.45

The conductivity tensor was approximately evaluated using a method similar to Rullmann's method (Rullmann et al., 2009); however, the grey matter, white matter and CSF regions were not separated in the 'inside the skull' region. We adjusted $\sigma_0 \sigma_{ru}$, $\sigma_0 \sigma_{rv}$ and $\sigma_0 \sigma_{rw}$ to the upper limit of V_U when this limit was exceeded so that the conductivity of CSF would not be exceeded. We also adjusted these values to a lower limit of 0.002 Sm^{-1}, which was one-tenth of V_L, when they were lower than this limit or negative.

Finally, the 'inside the skull' region adopted the evaluated tensor $\boldsymbol{\sigma}$ and the other regions adopted the isotropic average values of conductivities listed in Table 1.

4. Computing environment and settings for calculation

A personal computer running 64-bit Microsoft® Windows® 8.1 was used for the calculations. It had an Intel® Core™ i7–5960X CPU (8 CPU cores, 3 GHz) with 64 GiB of DDR4 SDRAM. The source code was compiled using Intel® Visual FORTRAN Compiler XE Ver. 15, with up to 16 OpenMP threads.

The order of the multipole and local expansions in the FMM algorithm was set to ten. The diagonal-form translation algorithm was used (Greengard & Rokhlin, 1997). The voxel cluster size used to define the leaf cell size of the FMM was $8 \times 8 \times 8$. The three-dimensional FFT was executed using the Intel® Math Kernel Library. The iterative solver used was GBi-CGSTAB(s, L) (Tanio & Sugihara, 2010), where $s = 1$ and $L = 1$. Convergence was assumed when the relative residual norm became less than 5.0×10^{-7}.

The applied homogeneous magnetic field, $\mathbf{B}_0 = (B_{0x}, B_{0y}, B_{0z})$, was 50-Hz AC. The vector potential was defined as $\mathbf{A}_0 = 0.5(B_{0y}z - B_{0z}y)\mathbf{i} + 0.5(B_{0z}x - B_{0x}z)\mathbf{j} + 0.5(B_{0x}y - B_{0y}x)\mathbf{k}$, and σ_0 was set to $1.0\ \mathrm{Sm}^{-1}$.

5. Results

5.1. Field analysis of rectangular solid conductor

In order to validate the proposed MoM, we calculated the electrostatic field in a homogeneous and anisotropic conductive rectangular solid. The dimensions of the conductor were $-0.1\ \mathrm{m} \leq x \leq 0.1\ \mathrm{m}$, $-0.07\ \mathrm{m} \leq y \leq 0.07\ \mathrm{m}$ and $-0.25\ \mathrm{m} \leq z \leq 0.25\ \mathrm{m}$. The voxel side length was set to 0.01 m. Therefore, this conductor is represented as a voxel model that does not include the shape representation error, which is sometimes called the staircase approximation error (Dawson et al., 1997; Hirata et al., 2010). Thus, we can confirm the validity of the MoM without incurring this type of error.

First, because an analytical solution of the induced field was available, the following settings were adopted: $\mathbf{u} = \mathbf{i}$, $\sigma_{ru} = \sigma_{rxx} = 8$, $\mathbf{v} = \mathbf{j}$, $\sigma_{rv} = \sigma_{ryy} = 4$, $\mathbf{w} = \mathbf{k}$, $\sigma_{rw} = \sigma_{rzz} = 2$, $\sigma_{rxy} = \sigma_{rxz} = \sigma_{ryz} = 0$, $\mathbf{B}_0 = B_{0z}\mathbf{k}$, and $B_{0z} = 1.0\ \mu\mathrm{T}$. The analytical solution is provided by the following equations (Wang & Eisenberg, 1994):

$$E_x = \frac{8\omega B_{0z}a}{\pi^2}\sqrt{\frac{\sigma_{ryy}}{\sigma_{rxx}}}\sum_{n=0}^{\infty}\left(\frac{(-1)^n}{(2n+1)^2}\cos(\alpha x)\frac{\sinh\left(\alpha y\sqrt{\sigma_{rxx}/\sigma_{ryy}}\right)}{\cosh\left(\alpha b\sqrt{\sigma_{rxx}/\sigma_{ryy}}\right)}\right), \quad (11)$$

$$\alpha = \frac{(2n+1)\pi}{2a},$$

$$E_y = \frac{-8\omega B_{0z}b}{\pi^2}\sqrt{\frac{\sigma_{rxx}}{\sigma_{ryy}}}\sum_{n=0}^{\infty}\left(\frac{(-1)^n}{(2n+1)^2}\cos(\beta y)\frac{\sinh\left(\beta x\sqrt{\sigma_{ryy}/\sigma_{rxx}}\right)}{\cosh\left(\beta a\sqrt{\sigma_{ryy}/\sigma_{rxx}}\right)}\right), \quad (12)$$

$$\beta = \frac{(2n+1)\pi}{2b},$$

where $2a$ and $2b$ are the side lengths of the rectangular solid in the x and y directions, respectively.

Furthermore, we calculated the induced field using a direct BEM that incorporates triangular patches. The fundamental solutions and the boundary integral equation are as follows (Brebbia & Dominguez, 1992):
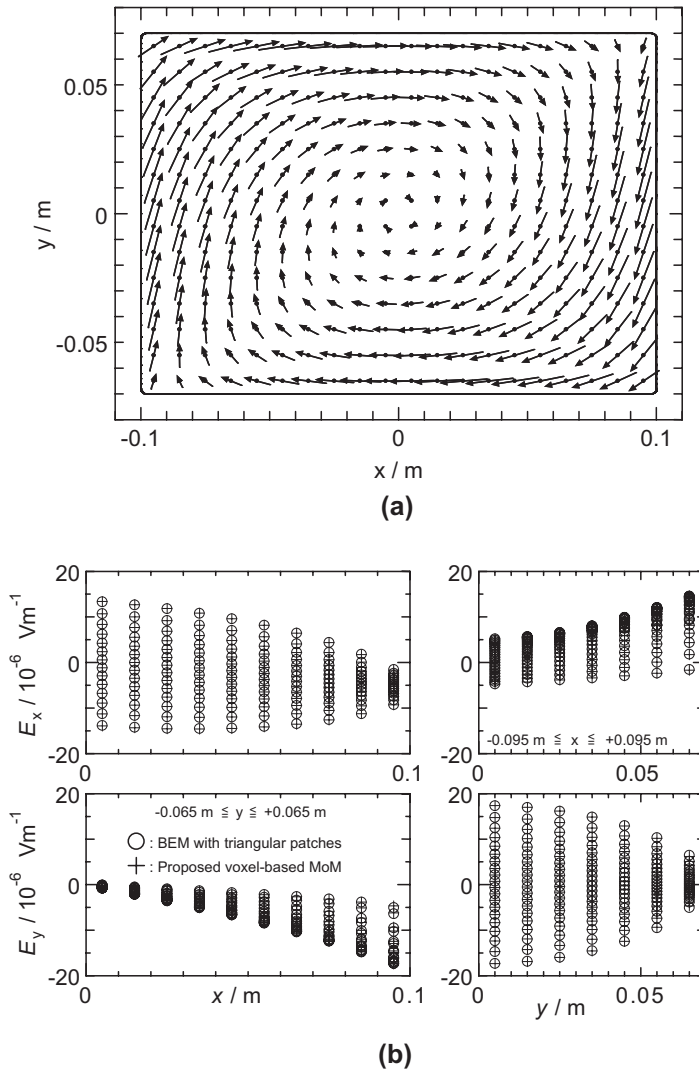
$$\varphi^*\left(\boldsymbol{r},\boldsymbol{r}_i\right) = \left(4\pi \sqrt{\sigma_{rv}\sigma_{rw}\left(u_i - u\right)^2 + \sigma_{rw}\sigma_{ru}\left(v_i - v\right)^2 + \sigma_{ru}\sigma_{rv}\left(w_i - w\right)^2} \right)^{-1},$$

(13)

(a)

(b)
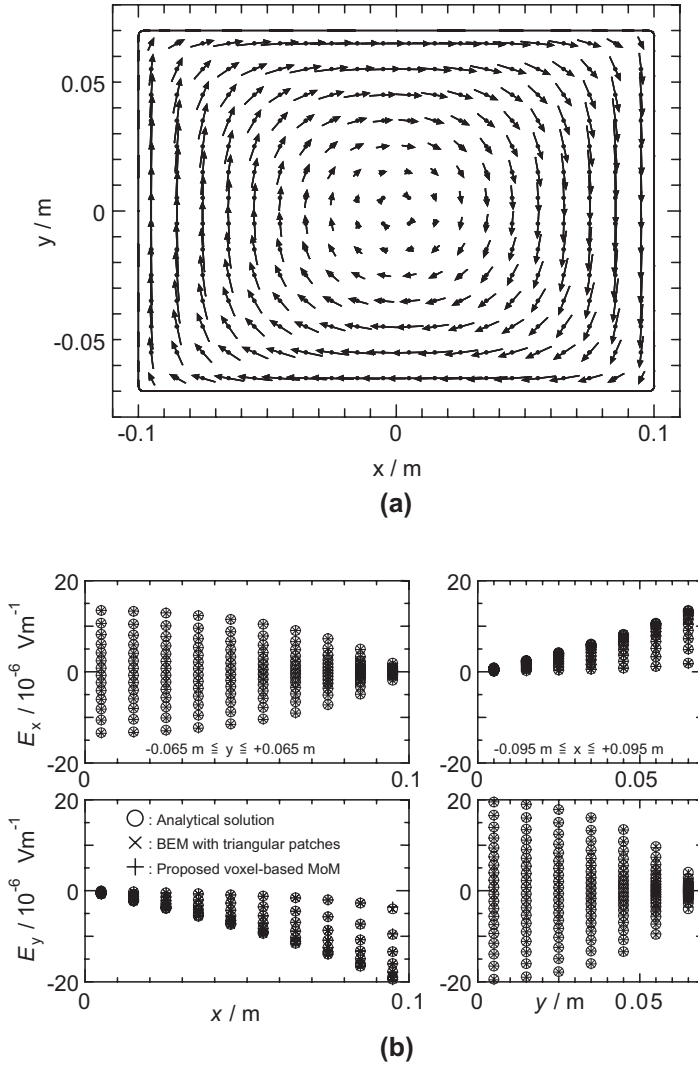
Figure 5. Electric fields in rectangular solid anisotropic conductor. Three arrows are drawn at each point in Figure 5(a), and the corresponding electric fields are calculated using the analytical equation, direct BEM and voxel-based static MoM, respectively. The electric fields corresponding to the circles, crosses and addition symbols in Figure 5(b) are also calculated using these respective methods.

$$q^*(\boldsymbol{r}, \boldsymbol{r}_i) = \sigma_{\mathrm{r}u} \frac{\partial \varphi^*(\boldsymbol{r}, \boldsymbol{r}_i)}{\partial u} \boldsymbol{u} \cdot \boldsymbol{n} + \sigma_{\mathrm{r}v} \frac{\partial \varphi^*(\boldsymbol{r}, \boldsymbol{r}_i)}{\partial v} \boldsymbol{v} \cdot \boldsymbol{n} + \sigma_{\mathrm{r}w} \frac{\partial \varphi^*(\boldsymbol{r}, \boldsymbol{r}_i)}{\partial w} \boldsymbol{w} \cdot \boldsymbol{n}, \quad (14)$$

$$\frac{c(\boldsymbol{r}_i)}{4\pi} \varphi(\boldsymbol{r}_i) = \int_S \varphi^*(\boldsymbol{r}, \boldsymbol{r}_i) q(\boldsymbol{r}) \mathrm{d}S - \int_S q^*(\boldsymbol{r}, \boldsymbol{r}_i) \varphi(\boldsymbol{r}) \mathrm{d}S, \quad (15)$$

Figure 6. Electric fields in rectangular solid anisotropic conductor. Two arrows are drawn at each point in Figure 6(a), and the corresponding electric fields are calculated using the direct BEM and voxel-based static MoM, respectively. The electric fields corresponding to the circles and addition symbols in Figure 6(b) are also calculated using these respective methods.

where $r = uu + vv + ww$ and $r_i = u_iu + v_iv + w_iw$ are position vectors on the boundary, n is the normal vector at r and $c(r_i)$ is a constant that depends on the boundary shape at r_i.

The number of conductive voxels and the number of unknowns were 14,000 and 87,960, respectively. The direct BEM used 21,674 unknowns. Figure 5(a) and (b) shows three types of electrostatic fields on a cross section for $z = -0.005$ m. However, it is difficult to distinguish the differences between them in Figure 5(a). Although we observe a slight decline in the accuracy of the MoM in the vicinity of the corners of the rectangular solid in Figure 5(b), the calculated fields are generally in good agreement.

Second, we randomly set the parameters to $\sigma_{ru}u = (9, 1.5, 3)$, $\sigma_{rv}v = (-1, 5, 0.5)$, $\sigma_{rw}w = u \times v$ and $B_0 = (0.4, 0.7, 1)$ μT. Figure 6(a) and (b) shows two types of electrostatic fields calculated using the direct BEM and the voxel-based MoM on a cross section for $z = -0.005$ m. However, the arrows at the same position in Figure 6(a) seem nearly identical. Although slight differences are observed in the vicinity of the corners of the rectangular solid in Figure 6(b), the calculated fields are in good agreement in practice. Therefore, we can conclude that the proposed method is valid.

5.2. Field analysis of simplified human head model constructed using DTI

5.2.1. Field analysis with simplified head model

In order to confirm the applicability of the proposed MoM to electrostatic field analysis of an anisotropic biological sample, we calculated the electrostatic field in the human head model described in Section 3 (see Figure 4 and Table 1) by applying the MoM and IBEM concurrently. The applied magnetic field was $B_0 = B_{0z}k$, with $B_{0z} = 1.0$ μT. The numbers of tissue voxels, unknowns, IBEM elements, one-sided elements and sextet charge elements are listed in Table 2.

Figure 7 shows the fractional anisotropy (FA; Wolters et al., 2006), $|J|$, and $|E|$ on four cross sections perpendicular to the z axis. FA is a frequently used index and is defined as

$$\mathrm{FA} = \left(\frac{3}{2} \frac{(\sigma_{ru} - \sigma_{rave})^2 + (\sigma_{rv} - \sigma_{rave})^2 + (\sigma_{rw} - \sigma_{rave})^2}{\sigma_{ru}^2 + \sigma_{rv}^2 + \sigma_{rw}^2} \right)^{1/2},$$

$$\sigma_{rave} = \frac{\sigma_{ru} + \sigma_{rv} + \sigma_{rw}}{3}. \tag{16}$$

Table 2. Specifications of head models and required costs of iterative solver.

| Model	Original (figure 4)	Finely subdivided (7^3) model
No. of tissue voxels	176,673	$60,598,839 = 7^3 \times 176,673$
No. of unknowns	606,277	188,296,465
No. of IBEM elements	48,925	$2,397,325 = 7^2 \times 48,925$
No. of one-sided elements	17,934	$878,766 = 7^2 \times 17,934$
No. of sextet charge elements	$539,418 = 6 \times 89,903$	$185,020,374 = 7^3 \times 539,418$
Time required by iterative solver	21.3 s	4968 s
Required C_x multiplications	180	216
Required amount of memory	0.5 GiB	50 GiB
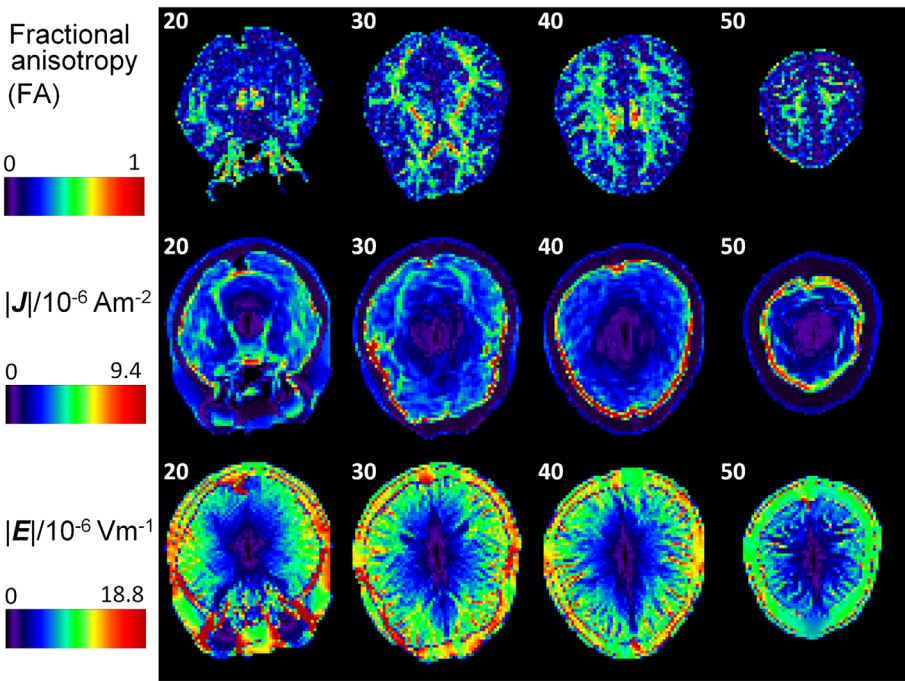
Figure 7. Calculated fields in simplified head model with inhomogeneous and anisotropic conductivity in the 'inside the skull' region. Numbers 20 through 50 indicate the z slice number.

This indicates the degree of anisotropy for a value from 0 to 1 (both inclusive). The upper row in Figure 7 shows the FA, which exhibits a nonzero value at an anisotropic conductive voxel. It is well known that the white matter region has structures of anisotropic nerve fibre bundles. Thus, the region represents inhomogeneous and anisotropic conductivity, which can be observed in the figure.

The middle row in Figure 7 shows the induced $|\boldsymbol{J}|$, which circulates in the same direction as the arrows in Figure 5 and has a large value in CSF because of its high conductivity. Furthermore, characteristically enhanced current flows are observed along the nerve fibre bundles, especially on the cross section for slice 30. Figure 8(a) shows the same slice with arrows that indicate the characteristic flows. These fibre bundles are the inferior fronto-occipital fasciculi and the inferior longitudinal fasciculi.

In order to gain a better understanding of this result, we calculated the field distribution in a variant of the original model, developed by replacing the conductivity tensors with inhomogeneous and isotropic conductivity of $\left(\left|\sigma_{ru}\sigma_{rv}\sigma_{rw}\right|\right)^{1/3}\sigma_0$ at every voxel in the 'inside the skull' region (see Figure 8(b)). Figure 8(b) shows that the current flows along the nerve fibre bundles, observed in Figure 8(a), disappear because of this replacement. In addition, we calculated the field distribution in another variant having a homogeneous and isotropic conductivity of $0.47\ \text{Sm}^{-1}$ in the 'inside the skull' region, as shown in Figure 8(c). The figure shows a smooth
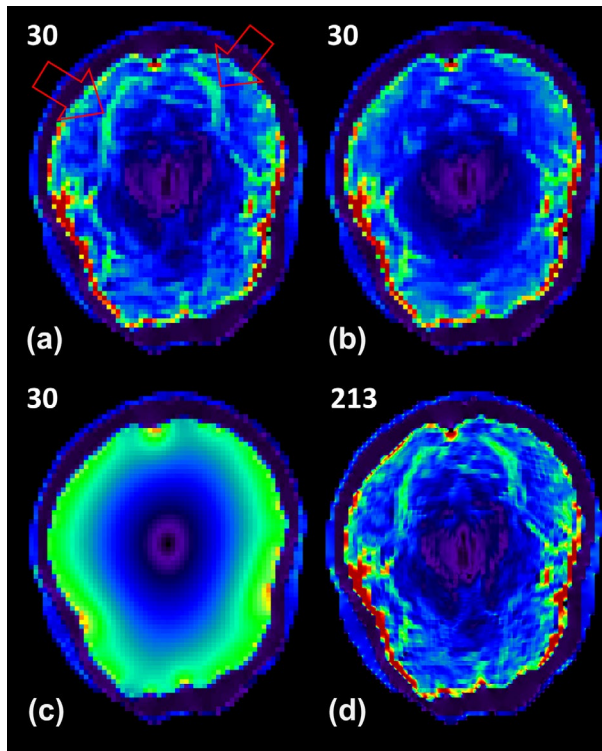
Figure 8. $|J|$ on slice 30 or on the corresponding cross section. The red arrows indicate the characteristic flows. (a) Original model with inhomogeneous and anisotropic conductivity (the same as that shown in Figure 7). (b) Variant with inhomogeneous and isotropic conductivity. (c) Variant with homogeneous and isotropic conductivity. (d) Subdivided model with inhomogeneous and anisotropic conductivity, each voxel volume of which is $1/7^3$ of the original one.

eddy field inside the region, and the detailed structures have disappeared. Thus, Figure 8(b) and (c) shows qualitatively reasonable results, as expected.

The lower row in Figure 7 shows the induced $|E|$, which roughly exhibits a radial stripe pattern. This appearance can be explained by the fact that the circulating J vertically crosses the layers of white matter, grey matter and the cerebral sulci filled with CSF. The conductivities of these layers are approximately 0.06, 0.1 and 2.0 Sm^{-1}, respectively, and J maintains a nearly constant intensity along the circulation path. Therefore, $|E| = |\sigma^{-1}J|$ repeats this rise and fall along the path.

5.2.2 Field analysis with finely subdivided head model

Because the conductivity tensors $\boldsymbol{\sigma}$ of all voxels in the 'inside the skull' region are estimated from the measured image data with relatively low signal-to-noise ratios, the tensors are discontinuous nearly everywhere. It was not clear whether we could obtain appropriate fields by analysing a model having such discontinuous $\boldsymbol{\sigma}$. Thus, we calculated the induced field in yet another variant, obtained by dividing each voxel into smaller voxels of equal volume ($7 \times 7 \times 7$) with the same $\boldsymbol{\sigma}$. Even

though the number of unknowns exceeds 188 million, the proposed method is able to manage such a relatively large-scale problem. The numbers of tissue voxels, unknowns and elements are listed in Table 2. The calculated $|J|$ is shown in Figure 8(d) on the cross section corresponding to slice 30 in Figure 8(a). A detailed distribution is observed in Figure 8(d), as compared to that in Figure 8(a), and the results in Figure 8(a) and (d) are macroscopically in good agreement. This result suggests that the field calculated in the original model is macroscopically useful.

The calculation times for solving the linear equations of the original and finely subdivided models are 21.3 and 4968 s, respectively (see Table 2). The respective numbers of required matrix-vector multiplications are 180 and 216. Thus, the ratio of single multiplication times is (4968 s/216)/(21.3 s/180) = 194.4. Further, the ratio of the respective numbers of unknowns is 188,296,465/606,277 = 310.6. These ratios roughly exhibit linear dependency as expected when using the FMM. Deviation from linearity is assumed to occur because the calculation time of 21.3 s is not fully optimised. The main memory requirements for analysing these models are around 0.5 and 50 GiB, respectively.

It has been shown that the proposed MoM and IBEM are concurrently applicable to field analyses of voxel models composed of isotropic and anisotropic tissues. Because each anisotropic tissue voxel consumes six surface elements, a small number of anisotropic tissue voxels and a large number of isotropic ones, which are addressed by the MoM and IBEM, respectively, are preferable. Although the method that approximates σ using DTI data requires further improvement to produce a more accurate estimation, it is an attractive method for using voxel models having both structural and property information extracted from MRI and DTI data.

6. Summary

A voxel-based static MoM was proposed to analyse electrostatic fields in biological tissues with anisotropic conductivities. The proposed method represents a cubic voxel of an anisotropic medium and a voxel cluster of an isotropic medium using a sextet of one-sided surface elements and one-sided surface elements, respectively. It does not execute volume integrals; thus, it is regarded as a type of IBEM. Therefore, the MoM can be concurrently applied with the voxel-based IBEM, and both methods can be accelerated by the FMM and FFT in the same manner.

After validating the MoM, we calculated the magnetically induced electrostatic fields in a simplified human head model constructed using DTI data. Through concurrent use of the proposed voxel-based MoM and the voxel-based IBEM, we succeeded in analysing voxel models composed of isotropic and anisotropic tissues. In addition, by analysing variants of the original inhomogeneous anisotropic model, we observed the variation in the electric current distributions in the following models: (i) an inhomogeneous isotropic model, (ii) a homogeneous isotropic model and (iii) an inhomogeneous anisotropic model with finer voxel

size. The calculated current distributions in these models showed qualitatively reasonable results. Furthermore, the proposed method could effectively manage 188,296,465 unknowns using a personal computer with an FMM-FFT hybrid algorithm.

Disclosure statement

No potential conflict of interest was reported by the author.

Funding

References

Brebbia, C. A., & Dominguez, J. (1992). *Boundary elements – An introductory course* (2nd ed.). (pp. 128–131). New York, NY: McGraw-Hill.

Cadebec, O., Coulomb, J. L., & Janet, F. (2006). A review of magnetostatic moment method. *IEEE Transactions on Magnetics, 42*, 515–520. doi:http://dx.doi.org/10.1109/TMAG.2006.870929

Dawson, T. W., Caputa, K., & Stuchly, M. A. (1997). Influence of human model resolution on computed currents induced in organs by 60-Hz magnetic fields. *Bioelectromagnetics, 18*, 478–490.

De Zaeytijd, J., Bogaert, I., & Franchois, A. (2008). An efficient hybrid MLFMA-FFT solver for the volume integral equation in case of sparse 3D inhomogeneous dielectric scatterers. *Journal of Computational Physics, 227*, 7052–7068. doi:http://dx.doi.org/10.1016/j.jcp.2008.04.009

Greengard, L., & Rokhlin, V. (1997). A new version of the fast multipole method for the Laplace equation in three dimensions. *Acta Numerica, 6*, 229–269. doi:http://dx.doi.org/10.1017/S0962492900002725

Hamada, S. (2011). GPU-accelerated indirect boundary element method for voxel model analyses with fast multiple method. *Computer Physics Communications, 182*, 1162–1168. doi:http://dx.doi.org/10.1016/j.cpc.2011.01.020

Hamada, S. (2014a). A voxel-based electrostatic field analysis for the virtual-human model Duke using the indirect boundary element method with a GPU-accelerated fast multipole method. *WIT Transactions on Modelling and Simulation, 57*, 135–147. doi:http://dx.doi.org/10.2495/BE370121

Hamada, S. (2014). Voxel-based analysis of electrostatic fields in virtual-human model Duke using indirect boundary element method with fast multipole method. *CMES: Computer Modeling in Engineering & Sciences, 102*, 407–424. doi:http://dx.doi.org/10.3970/cmes.2014.102.407

Hamada, S., & Kobayashi, T. (2006). Analysis of electric field induced by ELF magnetic field utilizing fast-multipole surface-charge-simulation method for voxel data. *IEEJ Transactions on Fundamentals and Materials, 126*, 355–362. doi:http://dx.doi.org/10.1541/ieejfms.126.355 (in Japanese) (translation: (2008). *Electrical Engineering in Japan*, 165, 1–10. doi:http://dx.doi.org/10.1002/eej.20529)

Hirata, A., Yamazaki, K., Hamada, S., Kamimura, Y., Tarao, H., Wake, K., … Fujiwara, O. (2010). Intercomparison of induced fields in Japanese male model for ELF magnetic field exposures:

Effect of different computational methods and codes. *Radiation Protection Dosimetry, 138*, 237–244. doi:http://dx.doi.org/10.1093/rpd/ncp251

Nagaoka, T., Watanabe, S., Sakurai, K., Kunieda, E., Watanabe, S., Taki, M., & Yamanaka, Y. (2004). Development of realistic high-resolution whole-body voxel models of Japanese adult males and females of average height and weight, and application of models to radio-frequency electromagnetic-field dosimetry. *Physics in Medicine and Biology, 49*, 1–15.

Newman, M. J., Trowbridge, C. W., & Turner, L. R. (1972). GFUN: An interactive program as an aid to magnet design. In *Proc 4th Int Conf Magnet Technology, Brookhaven* (pp. 617–626).

Rullmann, M., Anwander, A., Dannhauer, M., Warfield, S. K., Duffy, F. H., & Wolters, C. H. (2009). EEG source analysis of epileptiform activity using a 1 mm anisotropic hexahedra finite element head model. *NeuroImage, 44*, 399–410. doi:http://dx.doi.org/10.1016/j.neuroimage.2008.09.009

Takahashi, Y., Wakao, S., & Kameari, A. (2006). Large-scale and highly accurate magnetic field analysis of magnetic shield. *Journal of Applied Physics, 99*, 08H904. doi:http://dx.doi.org/10.1063/1.2172574

Tanio, M., & Sugihara, M. (2010). GBi-CGSTAB(s, L): IDR(s) with higher-order stabilization polynomials. *Journal of Computational and Applied Mathematics, 235*, 765–784. doi:http://dx.doi.org/10.1016/j.cam.2010.07.003

Wang, W., & Eisenberg, S. R. (1994). A three-dimensional finite element method for computing magnetically induced currents in tissues. *IEEE Transactions on Magnetics, 30*, 5015–5023. doi:http://dx.doi.org/10.1109/20.334289

Wolters, C. H., Anwander, A., Tricoche, X., Weinstein, D., Koch, M. A., & MacLeod, R. S. (2006). Influence of tissue conductivity anisotropy on EEG/MEG field and return current computation in a realistic head model: A simulation and visualization study using high-resolution finite element modeling. *NeuroImage, 30*, 813–826. doi:http://dx.doi.org/10.1016/j.neuroimage.2005.10.014

Appendix 1. Supplemental comments on procedures (i) and (ii) described in Section 2.

- Because the sextet of elements can handle anisotropic voxels, it can handle isotropic voxels as well. Although the non-conductive open region is isotropic, the one-sided elements are indispensable for representing this region.
- Because two one-sided elements in the same position are equivalent to an IBEM element, we can solve for unknown charge densities by using one-sided elements instead of conventional IBEM elements. In this case, we can skip procedure [ii].
- We can skip procedure [i] for the region where the relative conductivity σ_r is 1.0. Note that the relative conductivity of the non-conductive air region is 0.0.